THE JOURNAL OF PHYSICAL CHEMISTRY C

Article

Cite This: J. Phys. Chem. C 2019, 123, 25135−25145

pubs.acs.org/JPCC

Experimental Insights into the Genesis and Growth of Struvite Particles on Low-Solubility Dolomite Mineral Surfaces

Daniyal Kiani, Manoj Silva, Yiying Sheng, and Jonas Baltrusaitis*

Department of Chemical and Biomolecular Engineering, Lehigh University, B336 Iacocca Hall, 111 Research Drive, Bethlehem, Pennsylvania 18015, United States

ABSTRACT: Low-solubility Mg^{2+}-containing mineral surfaces, including periclase (MgO) and magnesite ($MgCO_3$), can act as sustainable sources of Mg^{2+} ions to yield green fertilizer struvite ($MgNH_4PO_4$) via a two-dimensional surface-facilitated growth. This work studied the kinetics, mechanism, and single-particle speciation of the natural mineral dolomite ($CaMg(CO_3)_2$) during struvite formation utilizing NH_4^+ and PO_4^{3-} ions from simulated wastewater. A range of $[Mg^{2+}]/[NH_4^+]/[PO_4^{3-}]$ ratios were tested and 0.69:1:1 [500/600 ppm of dolomite/monoammonium phosphate (MAP)] yielded the highest NH_4^+ removal efficiency of 37%. The highest PO_4^{3-} removal of 94% was obtained using ratio 1.37:1:1 (1000/600 ppm dolomite/MAP) but resulted in an amorphous solid phosphate phase rather than struvite. Moreover, significant compositional heterogeneities were observed in the spatially resolved ex situ single-crystal Raman spectroscopy with $CaCO_3$, $MgCO_3$, $MHPO_4$, and $M(H_2PO_4)_2$ (M: Mg or Ca) detected. Temporally resolved in situ Raman spectroscopy and spectrokinetic analysis provided mechanistic insights into the onset of the struvite crystal formation and growth. In particular, hydroxyl (OH) functional groups on the dolomite surface were consumed during CO_3^{2-} ion adsorption. The adsorbed CO_3^{2-} further served as adsorption sites for a combination of T_d symmetry PO_4^{3-}, C_{3v} HPO_4^{2-}, and C_{2v} $H_2PO_4^-$ in early stages of reaction. In the later stages, for example, during the onset of struvite crystal formation, adsorbed dimeric/polymeric $H_2PO_4^-$ units formed on the dolomite surface, which likely provide structural synergy at the solid−solution boundary for crystalline struvite nucleation and growth.

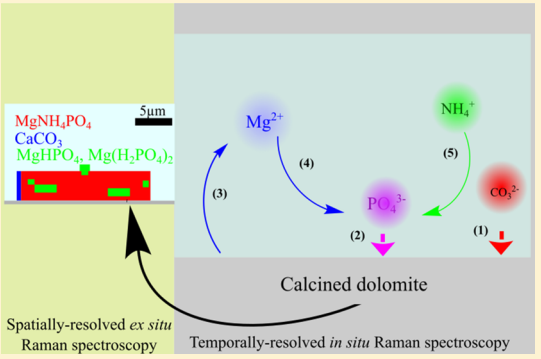

INTRODUCTION

The use of synthetic fertilizers has led to a significant alteration of the nitrogen (N) and phosphorus (P) global cycles due to the large influx of these critical plant nutrients into the environment.[1] Nitrogen fertilizers, although crucial to modern agricultural practices, are responsible for the emissions of ammonia (NH_3), potent greenhouse gas nitrous oxide (N_2O), and nitric oxides (NO_x).[2] Large fraction, anywhere from 50 to 90% of the applied fertilizer N, is converted into these gases via denitrification with soil bacteria.[3,4] On the other hand, phosphate ion-containing compounds are much less water-soluble and are transported into the watershed via runoff and erosion,[5] resulting in many environmental issues, such as eutrophication. The main source of P for mineral fertilizers is the phosphate rock available in limited, dwindling amounts,[6] which necessitates that P be recycled from the wastewater. Encapsulating N and P in a sparingly soluble crystalline form can provide slow-release green fertilizers containing these crucial nutrients, which can alleviate the environmental issues.[7] The availability of sustainable, low-solubility N and P fertilizers is essential in sustaining the population growth.[8]

Nutrient-laden wastewater can contain up to 1000 ppm ammonium (NH_4^+) ion and 5000 ppm (PO_4^{3-}) depending on its source.[9,10] Therefore, N and P containing anthropogenic wastewater provides a unique opportunity and the associated challenges in recovering nutrients in the form of a sparingly soluble solid struvite ($MgNH_4PO_4{\cdot}6H_2O$)[11,12] that can act as a green slow-release fertilizer. Traditionally, the crystallization of struvite from wastewater has been conducted via the addition of soluble magnesium salts, such as $MgCl_2$, and proceed via homogeneous nucleation.[13,14] Because of the unsustainable production of $MgCl_2$,[14,15] recent developments explored the use of low-solubility, naturally occurring Mg^{2+} sources, such as periclase (MgO)[10,16−18] or magnesite ($MgCO_3$).[16,19−22] Mechanistically, the work using MgO[10] identified key findings where PO_4^{3-} removal occurred in two MgO concentration regimes with an equilibrium regime of 300 ppm MgO ($[Mg/NH_4^+/PO_4^{3-}]$ of 1.44:1:1) and a kinetic regime with 1000 ppm MgO ($[Mg/NH_4^+/PO_4^{3-}]$ of 4.80:1:1), both leading to struvite product and >70% NH_4^+ removal from solution. Further, the formation of a reactive intermediate dypingite ($Mg_5(CO_3)_4(OH)_2{\cdot}5H_2O$) via hydration at ambient conditions was identified as the reactive step preceding PO_4^{3-} adsorption.[10] This prompted a study using $MgCO_3$ as a precursor to struvite due to its structural proximity to dypingite. Results obtained using $MgCO_3$[19] demonstrated that it removed NH_4^+ and PO_4^{3-} to form struvite while also revealed that the presence of Ca^{2+} from either insoluble source

Received: June 4, 2019
Revised: September 19, 2019
Published: September 24, 2019

DOI: 10.1021/acs.jpcc.9b05292
J. Phys. Chem. C 2019, 123, 25135−25145

($CaCO_3$) and soluble ($CaCl_2$) sources had different effects on struvite formation pathways and its final single-particle composition.[19] The use of $CaCl_2$ led to an inhibitory behavior toward struvite formation and poor crystallinity calcium hydroxyapatite crystal formation while $CaCO_3$ did not exhibit the same effect and led to struvite crystals.[19] Lastly, a recent report utilized a rather complex mineral surface dolomite ($CaMg(CO_3)_2$) to synthesize struvite crystals.[23] However, little fundamental insights into the growth kinetics and mechanisms were provided. Hence, struvite formation using sparingly soluble Mg-mineral surfaces proceeds via intriguing heterogeneous nucleation chemistry, which needs to be further studied to elucidate key mechanistic details.

In this work, dolomite was utilized as the Mg^{2+} source because it is little studied mineral for struvite synthesis despite being abundant.[24,25] Dolomite is a double-carbonate mineral composed of Ca^{2+} and Mg^{2+} cation−CO_3^{2-} anion pairs[25] in a very stable lattice and calcination at high temperatures results in dolomite decomposition into a mixture of MgO, CaO, and $CaCO_3$.[23,26−30] The solubility of dolomite in water is very low (pK_{sp} value of 17.00),[31] lower than MgO[32−36] and $CaCO_3$[37] with reported pK_{sp} values of 10.86[36] and 8.07,[37] respectively. Because dolomite can act as a source of Ca^{2+} along with Mg^{2+} and it is known that the presence of Ca^{2+} can hinder struvite formation[38] or replace Mg^{2+} in struvite to form Ca-struvite,[19] the use of dolomite for struvite synthesis from wastewater presents an interesting challenge. For this reason, insights into the observed reaction kinetics, crystal formation onset and nucleation, and the growth mechanisms of struvite using dolomite are reported using a multimodal approach. Temporally resolved, in situ Raman spectroscopy and spectrokinetic analysis were used to elucidate the genesis of the molecular species in the first few layers of the dolomite surface at the solid−solution boundary. Ex situ single-particle Raman spectroscopy was used to assess the detailed compositional heterogeneity of the resulting crystals. Ion chromatography (IC) was utilized to assess the observed kinetics of aqueous ion adsorption/reaction while powder X-ray diffraction (pXRD) was used for bulk solid-phase identification.

EXPERIMENTAL METHODS

Ion Chromatography. The Metrohm Eco 925 IC system (Herisau, Switzerland) was used in all experiments. Separation columns used were Metrosep A supp 4/5 Guard column (5 × 4 mm), Metrosep A supp 5 (4 × 150 mm) for anion analysis and Metrosep C 4 Guard column (5 × 4 mm), Metrosep C 4 (4 × 150 mm) for cation analysis. The sample-loop volume was 10 μL in the cation system and 20 μL in the anion system, and eluted species were measured using a conductivity detector. Dipicolinic acid (1.75 nM HNO_3/0.7 mM) was used as an eluent for Metrosep C 4 while 3.2 mM Na_2CO_3/1.0 mM $NaHCO_3$ for Metrosep A supp 5. All samples were measured at room temperature. The system was computer-controlled through MagIC Net 3.2 software.

Powder X-ray Diffraction. The crystalline nature of all reactants and products was confirmed using pXRD (Empyrean, PANalytical B.V.). The applied current was 40 mA, and the applied voltage was 45 kV. The X-ray mirror that was used was a graded, flat Bragg−Brentano HD mirror, and the step size that was used for the measurements was 0.0131°. The diffraction patterns were obtained between 20 and 75°. The radiation source used was Cu $K\alpha_{1,2}$ with Cu $K\alpha_1$ wavelength 1.540598 Å and Cu $K\alpha_2$ wavelength 1.544426 Å. The ratio of $K\alpha_1/K\alpha_2$ was 0.5. The analysis was performed with a 4 mm mask, 1/8″ incident beam divergence slit, 1/2″ incident beam anti-scatter slit, 7.5 mm diffracted beam anti-scatter slit, and a 0.04 mm Soller slit. In all cases, the powder was placed on a glass slide and pressed into a 1 cm × 1 cm sized smooth powder film.

Raman Spectroscopy. Raman spectra and spectral maps were acquired using a WITec alpha300R confocal Raman microscope using a 532 nm laser, Zeiss EC Epiplan-Neofluar ×100/0.9 objective, G2:600 g/mm grating, 3 s integration time per point for ex situ study. For in situ studies, a 532 nm laser, Zeiss ×20/0.4 objective, and G2:600 g/mm grating was used. In both studies, the spectral range was 100−4000 cm^{-1} with the center at 2000 cm^{-1} and the spectral resolution was ∼2 cm^{-1}. Before each experiment, the instrument was calibrated using a Si wafer. A specially designed polylactic acid 3-D printed cell shown in Figure 1 was utilized for the in situ study.

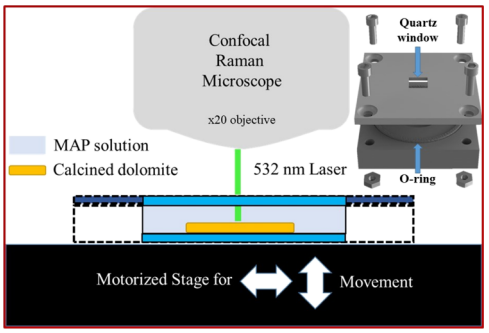

Figure 1. Schematic of the in situ Raman cell utilized for the study.

Laser intensity at the sample was ∼54 mW. Spectral maps were typically acquired using 2−4 s exposure time per single scan point. To elucidate heterogeneity of a single particle, 2-D spectral maps were acquired in the $x-z$ plane, for example, parallel to the direction of the beam.

Reagents and Solutions. A stock solution of ammonium (1.0000 g/L) and phosphate (1.0000 g/L) were prepared from monoammonium phosphate, $NH_4H_2PO_4$ (MAP, 99.9%+, Fisher Scientific). Finely dolomite powder was obtained from Omya (Agrodol-65D-SA, <150 μm, St. Armand, Canada). Appropriate amounts of individual salts were weighed into a volumetric flask (100 mL) and dissolved in deionized (DI) water. Working standard solution of ammonium, magnesium, and phosphate were prepared by measuring the appropriate volume of standard solutions into a 100 mL volumetric flask, which was later filled to the mark with DI water. Working eluent solutions were prepared by appropriate dilution of standard eluent solution with DI water. DI water (18.2 MΩ/cm, Millipore, Bedford, MA, USA) was used for dilution in all cases.

Struvite Synthesis. The struvite synthesis from simulated wastewater was performed using dolomite. Simulated NH_4^+ and PO_4^{3-} containing wastewater samples were prepared by adding 600 ppm of MAP ($NH_4H_2PO_4$, Fisher Scientific, Certified A.C.S.) at room temperature under constant stirring at 350 rpm. MAP (600 ppm) represents PO_4^{3-} and NH_4^+ values found in municipal, animal, and industrial wastewater[9] while maintaining molar 1:1 ratio needed for struvite formation. Dolomite was added at concentrations from 300 to 1000 ppm to the simulated wastewater and stirred for up to 120 min. The Mg^{2+} concentration in dolomite was calculated

DOI: 10.1021/acs.jpcc.9b05292
J. Phys. Chem. C 2019, 123, 25135−25145

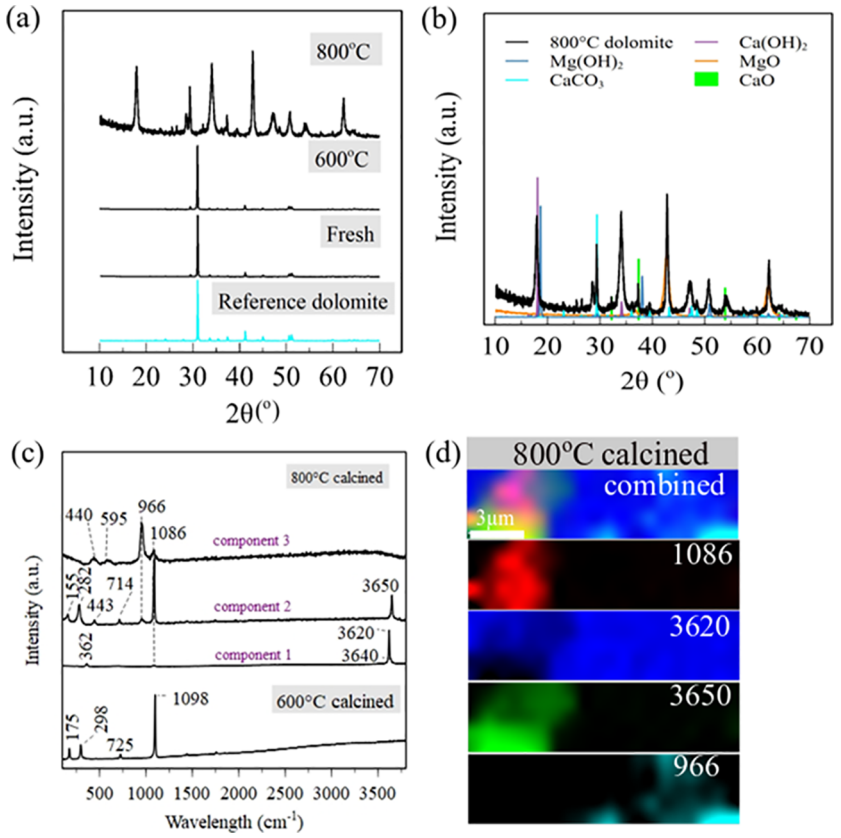

Figure 2. (a) pXRD patterns of dolomite calcined at different temperatures (reference, uncalcined, calcined at 600 and 800 °C), (b) pXRD patterns of dolomite calcined at 800 °C, with reference XRD patterns of possible carbonates, oxides, and hydroxides obtained from RUFF database (MgO,[58] $CaCO_3$,[59] $Mg(OH)_2$,[60] $Ca(OH)_2$,[61] and CaO[62]). (c) TCA of the unique Raman spectral components of dolomite calcined at 600 and 800 °C and (d) relative intensity peak maps of dolomite after calcination at 800 °C.

on the basis of calcined dolomite that was assumed to be comprised of MgO and $CaCO_3$.[23] The total volume of reactive solution was 500 mL. Solution (1 mL) was sampled periodically, filtered through a 13 mm polyethersulfone filter (0.22 μm size) to remove solid material, and analyzed using IC. The dolomite concentrations used for struvite synthesis were 300, 500, and 1000 ppm, which correspond to molar $[Mg^{2+}]/[NH_4^+]/[PO_4^{3-}]$ ratios of 0.41:1:1, 0.69:1:1, and 1.37:1:1. $[Mg^{2+}]/[NH_4^+]/[PO_4^{3-}]$ ratios of 0.5−1.5:1:1 have previously been tested and was concluded that lower ratios lead to a lesser N and P adsorption/reaction.[18,39−41] Therefore, a slight excess of Mg^{2+} was preferred in the previous works to circumvent this issue and ensure efficient removal of N and P from the solution.[41,42]

PO_4^{3-} Adsorption Kinetics. Pseudo-second-order[43] kinetic models were used to analyze the obtained PO_4^{3-} adsorption data. In particular, the kinetic model parameters obtained by a linear plot of t/q_t versus t for pseudo-second-order model (1) was used

$$t/q_t = 1/k_2 q_e^{\ 2} + t/q_e \quad (1)$$

where q_t (mg g^{-1}) and q_e (mg g^{-1}) are the amounts of PO_4^{3-} adsorbed at time t (h) and at equilibrium, respectively. k_2 (g mg^{-1} min^{-1}) is the rate constant of pseudo-second-order kinetic models, respectively. The error bars are based on three independent measurements for each data point.

RESULTS AND DISCUSSION

Spectroscopic Analysis of Dolomite before and after Calcination. The dolomite structure can be described either as a combination of alternating calcite- and magnesite-like layers or as substitution of Mg^{2+} atoms for the Ca^{2+} atoms in every other cation layer.[44] The C−O bond length in dolomite is that of typical calcite-like carbonate minerals. However, the Ca−O bond length is 2.38 Å, whereas the Mg−O bond length is 2.08 Å, that is, the oxygen atoms in threefold coordination are closer to Mg than Ca in the lattice.[44] For these reasons, dolomite is known as a recalcitrant mineral with low reactivity.[23]

Dolomite was subjected to high-temperature treatment and changes in the crystalline structure were monitored using ex situ pXRD and Raman spectroscopy. Calcination at temperatures up to 600 °C did not show any change in pXRD patterns, as shown in Figure 2a. However, after calcining at 800 °C, significant changes were observed. After calcining at 800 °C, the resulting solid exhibited a complex XRD pattern, which was found to be a combination of CaO, MgO, $Ca(OH)_2$, $Mg(OH)_2$, $CaCO_3$, as shown in Figure 2b. The resulting complex mixture after thermal decomposition in our study is in line with literature reports, which also observed complex solid mixtures forming during dolomite calcination.[45−47] For example, one study found that dolomite decomposition involved the initial formation of mixed oxide ($Ca_{0.5}Mg_{0.5}O$), whereas at T > 500 °C decomposition preferentially formed CaO and MgO.[45] At even higher temperatures of 650−750 °C, nanocrystals of Mg-calcite were also detected.[45] Likewise,

DOI: 10.1021/acs.jpcc.9b05292
J. Phys. Chem. C 2019, 123, 25135−25145

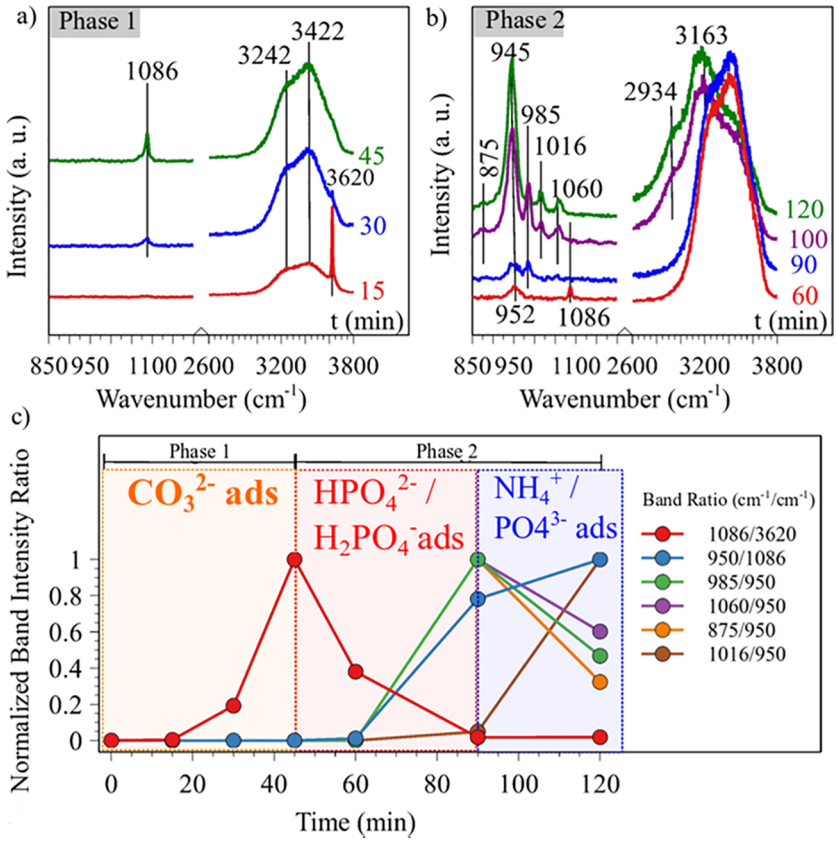

Figure 3. Temporally resolved in situ Raman spectra of molecular speciation prior to and during struvite formation using 500/600 ppm dolomite/MAP: (a) phase 1 (0−45 min) before PO_4^{3-} and NH_4^+ adsorption (red—15 min, blue—30 min, green—45 min), (b) phase 2 (60−120 min) during PO_4^{3-} and NH_4^+ adsorption (red—60 min, blue—90 min, purple—100 min, green—120 min). (c) Resulting spectrokinetics data calculated for peaks in (a,b).

other studies detected a mixture of MgO, CaO, $Ca(OH)_2$, and $CaCO_3$ post calcination.[46,47] Interestingly, a few studies have also argued that Mg in $CaMg(CO_3)_2$ moves to the surface to release CO_2 gas, which leads to the external growth of MgO and the internal growth of $CaO/CaCO_3$, meaning that the calcined dolomite surface is Mg-rich.[46,47]

It was observed that no struvite particles formed using as-received dolomite or dolomite calcined up to 600 °C in the presence of 600 ppm MAP solution, even at an extended reaction time of 120 min, which has been shown as sufficient to achieve aqueous NH_4^+ and PO_4^{3-} adsorption/reaction equilibrium.[10,19] Provided that the parent dolomite is a carbonate mineral, this low reactivity was intriguing, as magnesium carbonates typically react more readily in aqueous conditions because their hydration is less complex, unlike hydration of the corresponding alkali metal oxide, such as MgO and CaO.[19] The surface of the 800 °C calcined dolomite prior to the reaction with NH_4^+ and PO_4^{3-} was probed using Raman spectroscopy to elucidate the surface structural and chemical information. The corresponding Raman spectrum of dolomite calcined at 600 and 800 °C are shown in Figure 2c. Fresh dolomite and calcined up to 600 °C exhibited characteristic dolomite Raman bands at 177, 298, 725, 1098, 1440, and 1756 cm^{-1}, which match Raman spectra reported in the literature for dolomite.[48,49] On the other hand, the total component analysis of spatially resolved Raman spectroscopic characterization of dolomite calcined at 800 °C exhibited three unique spectra, shown in Figure 2c component one exhibited bands at 362, 1086, and 3620 cm^{-1}. Two weak, broad bands at ~263 and 690 cm^{-1} are not labeled in the figure but were also present. The 1086 cm^{-1} band corresponds to the ν_1 of CO_3^{2-} in calcite ($CaCO_3$),[19,49−53] whereas the ~263, 362, ~690, and 3620 cm^{-1} bands correspond to $Ca(OH)_2$.[50,51] For component two, the bands at 155, 282, 714, and 1086 cm^{-1} match those of $CaCO_3$,[19,49−53] confirming the presence of $CaCO_3$ in the 800 °C calcined sample. Moreover, the 443 and 3650 cm^{-1} bands in component two correspond to the $Mg(OH)_2$ phase.[54,55] Lastly, component three exhibited a 1086 cm^{-1} band, which corresponds to $CaCO_3$ phase, whereas the other three bands in this component at 440, 595, and 966 cm^{-1} did not match any of carbonate, oxide, or hydroxide phases. We tentatively assign these Raman bands to a phosphate or silicate impurity because Raman bands for PO_4^{3-} are at ~447 (ν_2), 580−620 (ν_4), and ~961 cm^{-1} (ν_1),[56,57] whereas those for silicate wollanstonite with the main peak at 966 cm^{-1}, cyan in Figure 2d, were also reported.[57] The spatially resolved unique peak intensity maps, constructed by tracking relative intensities of unique Raman peaks for each phase, that is, $CaCO_3$ (1086 cm^{-1}), $Mg(OH)_2$ (3650 cm^{-1}), $Ca(OH)_2$ (3620 cm^{-1}) and an impurity (966 cm^{-1}) are shown in Figure 2d. The maps show that the majority of the scanned area is dominated by the $Ca(OH)_2$ phase (3620 cm^{-1}, blue), whereas a small area is co-populated by $Mg(OH)_2$ and $CaCO_3$ (3650, green and 1086 cm^{-1}, red, respectively).

Temporally Resolved in Situ Raman Characterization of Struvite Formation on Dolomite Calcined at 800 °C. A specially designed 3D-printed cell with quartz window was used to conduct temporally resolved in situ Raman character-

DOI: 10.1021/acs.jpcc.9b05292
J. Phys. Chem. C 2019, 123, 25135−25145

ization during the reaction of 600 ppm MAP ($NH_4H_2PO_4$) solution with the 800 °C calcined dolomite particle surface under diffusion-limited conditions to generate preliminary mechanistic insights into struvite crystallization on dolomite surfaces. The dolomite/MAP concentrations were 500:600 ppm, which correspond to a molar ratio $Mg^{2+}/NH_4^+/PO_4^{3-}$ of 0.69:1:1. Previous studies have shown that $Mg^{2+}/NH_4^+/PO_4^{3-}$ molar ratios of 0.5−1.5:1:1 have resulted in N and P adsorption/reaction to form struvite.[18,39−41] The results of the temporally resolved in situ Raman analysis of the diffusion-limited reaction of MAP with 800 °C calcined dolomite are shown in Figure 3a,b. The sample area was selected to contain typical hydroxyl groups at 3620 cm^{-1}. The collected in situ Raman data are plotted in two panels, each representing a distinct temporal phase of speciation during the struvite formation with 0−45 min spectral components in (a) and 60−120 min spectral components in (b). The spectra acquired after 15 and 30 min, shown in red and blue in Figure 3a, exhibited a very weak band at 1086 cm^{-1}, a broad band in the 3200−3800 cm^{-1} region with shoulders at 3242 and 3422 cm^{-1} and an intense, sharp band at 3620 cm^{-1}. As explained previously, the band at 1086 cm^{-1} corresponds to the ν_3 antisymmetric stretch of the CO_3^{2-}, whereas the 3620 cm^{-1} corresponds to stretching vibration of the −OH in $Ca(OH)_2$.[19,50,51] The broad band with shoulders at 3242 and 3422 cm^{-1} can be attributed to the −OH stretching in H_2O molecules in the proximity of the surface.[63,64] The Raman spectrum acquired after 45 min (shown in green) exhibited a much more intense band at 1086 cm^{-1}, whereas the 3620 cm^{-1} band was absent, suggesting −OH units had been depleted, that is, likely CO_3^{2-} groups were generated on the surface at the expense of the −OH groups.

Figure 3b shows in situ Raman spectra acquired from 60 to 120 min of the reaction time. After 60 min (red spectrum), a weak, broad band at 952 cm^{-1} corresponding to ν_1 mode of PO_4^{3-} surface species, a band at 1086 cm^{-1} corresponding to the ν_3 antisymmetric stretch of the CO_3^{2-} in $CaCO_3$, and a broad band in 3200−3800 cm^{-1} region corresponding to the −OH stretching in surface H_2O[63] were observed. After 90 min (blue spectrum Figure 3b), an additional band at 985 cm^{-1} appeared, which we assigned to ν_1 symmetric stretch of PO_4 unit in HPO_4^{2-}.[65,66] The adsorption of HPO_4^{2-} agrees with a previous report[67] and likely occurs at an Mg-surface site. At 100 min (purple spectrum Figure 3b), additional bands at 875, 1016, and 1060 cm^{-1} appeared and were assigned to a combination of PO_4^{3-} and $H_2PO_4^-$ stretches,[65,68] whereas the new shoulders at 2934 and 3163 cm^{-1} corresponded to N−H vibrations from the adsorbed NH_4^+ species.[10,19] Lastly, at 120 min (green spectrum Figure 3b), no additional bands were observed; however, the 952 cm^{-1} band shifted to 945 cm^{-1} and intensified compared to all other bands in the phosphate region (i.e. 875, 985, 1016 and 1060 cm^{-1}), suggesting growth in the relative population of the T_d symmetry PO_4^{3-} species, when compared to C_{3v} symmetry HPO_4^{2-} and C_{2v} symmetry $H_2PO_4^-$ species. Note that in aqueous solutions, the PO_4^{3-} anion has an intense band at 936 cm^-,[164,65] whereas Raman bands corresponding to the HPO_4^{2-} anion in aqueous solutions are at 855−875 cm^{-1} (ν mode of P−OH) and 985−995 cm^{-1} (ν_1 symmetric stretch of PO_4 unit in HPO_4^{2-}).[64,65] Lastly, the Raman spectrum of the $H_2PO_4^-$ anion in aqueous environment exhibits three bands at 855−878 cm^{-1} (ν mode of P−OH), 985−995 cm^{-1} (ν_1 symmetric stretch of PO_4 unit in $H_2PO_4^-$), and 1077 cm^{-1} because of P−O vibrations.[65] Correspondingly, it is known that the Raman spectra of the PO_4^{3-} anions will alter as hydrogen is attached to the PO_4^{3-}, that is additional Raman bands will be observed as the symmetry of the T_d (PO_4^{3-}) is lowered to C_{3v} (HPO_4^{2-}) and further to C_{2v} ($H_2PO_4^-$), which we propose was observed in this in situ Raman study.

A qualitative spectrokinetic analysis of the temporally-resolved Raman spectra further aids in understanding the genesis of different molecular species during struvite formation. Such a spectrokinetic approach has been previously employed to understand material transformations, structural disorder, and molecular structures.[69−72] Herein, relevant Raman band intensity ratios were constructed and analyzed as a function of time. The numerator band is chosen such that it evolved temporally after the band chosen as the denominator, that is, in the case of 950/1086 cm^{-1}, the 950 cm^{-1} band appeared as the 1086 cm^{-1} band started disappearing, suggestive of the product-like nature of the numerator and reactant-like nature of the denominator. Initially, CO_3^{2-} adsorption (from ambient CO_2 dissolution and reaction with the −OH units)[73,74] rate increased, as seen from the increasing slope of the 1086/3620 cm^{-1} band intensity ratio during the initial 45 min, as shown in Figure 3c. Subsequently, in the early stages of phase 2 (45−90 min), the CO_3^{2-} species started to diminish until fully depleted, highlighting the transient nature of these surface species. Simultaneously with the CO_3^{2-} depletion, PO_4^{3-} species started to adsorb on the surface, presumably on the same reactive sites that previously anchored the CO_3^{2-}, as seen by the positive slope of 950/1086 cm^{-1}. Moreover, the HPO_4^{2-} and $H_2PO_4^-$ species, represented by intensity ratios of 875/950, 985/950, and 1060/950 cm^{-1} bands, increased in the early stages of phase 2, as indicated by the positive slope of the band ratios. However, in later stages of phase 2 (90−120 min), a decrease in HPO_4^{2-} and $H_2PO_4^-$ species was observed on the top layers of the material being analyzed, as signified by the negative gradients of the intensity ratios of 875/950, 985/950, and 1060/950 cm^{-1} bands. This suggests that early nucleation layers formed during reaction contained HPO_4^{2-} and $H_2PO_4^-$ species, which might be serving as the nucleation sites for further adsorption of PO_4^{3-} and NH_4^+ ions to form the struvite crystal lattice. Interestingly, the PO_4^{3-} adsorption was faster in the early stages of phase 2 than the later stage, as indicated by a smaller slope of the 950/1086 cm^{-1} band beyond 90 min. Last, the 1016 cm^{-1} band, attributed to the symmetric PO_4^{3-} stretching appeared in conjunction with 2934, 3163 cm^{-1} NH_4^+ bands. The intensity ratio of 1016/950 cm^{-1} bands increased in the latter half of phase 2 most likely as simultaneous adsorption of NH_4^+, PO_4^{3-} and Mg^{2+} species occurred and the struvite crystal lattice began to form. Hence, the Raman spectroscopic evidence provided herein regarding a two-phase genesis model suggests that CO_3^{2-} adsorption takes place on −OH units, followed by CO_3^{2-} depletion, as PO_4^{3-} species replace them. Also, early growth stages have higher population of HPO_3^{2-} and $H_2PO_4^-$ species, which decreases as struvite lattice begins to grow and PO_4^{3-}, NH_4^+, and Mg^{2+} species start coordinating on to these layers. These in situ experiments were performed without mixing, for example, under mass transfer-limited conditions to observe the corresponding speciation and evolution. However, the mechanism and temporal evolution of the intermediate species likely does not change under stirring that was used to measure the overall process kinetics in bulk experiments (vide infra).

DOI: 10.1021/acs.jpcc.9b05292
J. Phys. Chem. C 2019, 123, 25135−25145

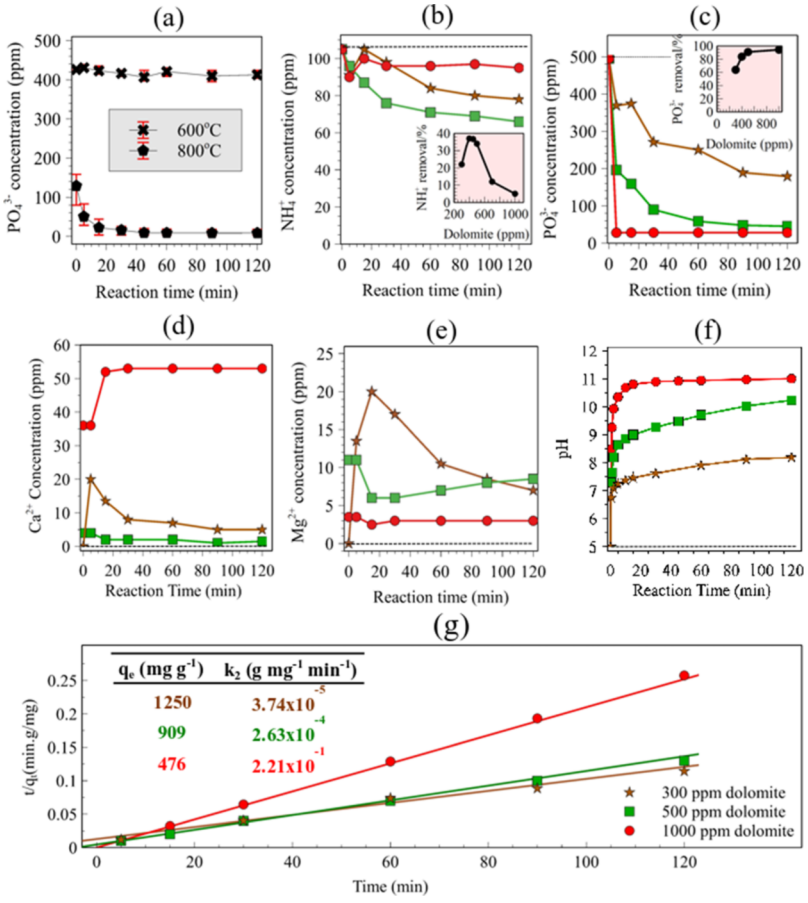

Figure 4. Ion concentration as a function of reaction time, measured using IC (a) PO_4^{3-} concentration for reaction with dolomite calcined at 600 and 800 °C, with standard deviation shown as error bars for selected time points (b) NH_4^+ concentration, (c) PO_4^{3-} concentration, (d) Ca^{2+} concentration, (e) Mg^{2+} concentration, (f) pH change over time, (g) pseudo-second-order kinetic fit results. Note: The dotted black lines in Figure 4b,c,d,e,f indicate initial concentrations and pH.

Kinetic Studies of Struvite Formation Using Dolomite Calcined at 800 °C. IC was used to measure the time-dependent concentrations of residual anions (PO_4^{3-}) and cations (Mg^{2+}, NH_4^+, and Ca^{2+}) in solution under reaction limited conditions. Although dolomite calcined at 800 °C showed highs PO_4^{3-} removal, the 600 °C treated dolomite led to almost no PO_4^{3-} removal, as shown in Figure 4a. For kinetic studies, three concentrations of dolomite were used, as Mg^{2+} concentration is known to affect struvite yield and the corresponding kinetics.[10,19] These concentrations were 300, 500, and 1000 ppm dolomite, which correspond to molar $[Mg^{2+}]/[NH_4^+]/[PO_4^{3-}]$ ratios of 0.41:1:1, 0.69:1:1, and 1.37:1:1, respectively. The time-dependent concentration of NH_4^+ ions in the solution is shown in Figure 4b, with the inset showing the total NH_4^+ removal after the 2 h reaction period. 1000 ppm dolomite exhibited some initial reactivity but equilibrated to 95 ppm NH_4^+, resulting in only 5% overall NH_4^+ removal from the solution. Similar transient behavior was also observed for 1000 ppm MgO where initial NH_4^+ removal was observed, followed by the release back into solution in a previous study.[10] However, at lower concentrations of dolomite, it was observed that unlike MgO and $MgCO_3$,[10,19] dolomite did not result in high (>80%) NH_4^+ removal. The highest NH_4^+ ion removal of 37% was observed for 500 ppm. The removal of NH_4^+ ions from solution shows a maximum as a function of increasing dolomite concentration, which differs significantly from the behavior seen in prior work with $MgCO_3$, but similar to the behavior seen with MgO[10,19] suggesting that similar sites are most likely responsible for the underlying reactivity. Figure 4c shows the change in the PO_4^{3-} concentration as a function of the reaction time for dolomite of 300, 500, and 1000 ppm. While all three concentrations resulted in the PO_4^{3-} removal, the 1000 ppm dolomite concentration showed the fastest reaction rate and percent ion removal at 94.35% as shown in the inset figure. The 1000 ppm dolomite resulted in a final PO_4^{3-} concentration of 28 ppm, while 500 ppm dolomite resulted in the final concentration of 45 ppm. 300 ppm dolomite resulted in the lowest PO_4^{3-} reaction with a final concentration of 179 ppm. Figure 4d,e show the time-dependent cation concentrations (Mg^{2+} and Ca^{2+}) during the struvite precipitation experiments. In 300 and 500 ppm dolomite loadings, the final cation concentrations in the solution were less than 20 ppm. The pH change with time shown in Figure 4f exhibits similar trends to the ones reported in a previous study using $MgCO_3$.[19] Increasing the dolomite concentration in solution led to an increase in pH from the initial 4.9 for pure 600 ppm MAP. In the 300 ppm case, the pH increased to 8.19, whereas in 500 and 1000 ppm the pH increased to 10.24 and 11.01, respectively, after 2 h. Importantly, the Mg^{2+} concentration measured in solution is only a fraction of that in the bulk dolomite. This suggests that Mg^{2+} ions never fully dissolve to undergo homogeneous struvite nucleation and growth but rather are mobilized in the

DOI: 10.1021/acs.jpcc.9b05292
J. Phys. Chem. C 2019, 123, 25135−25145

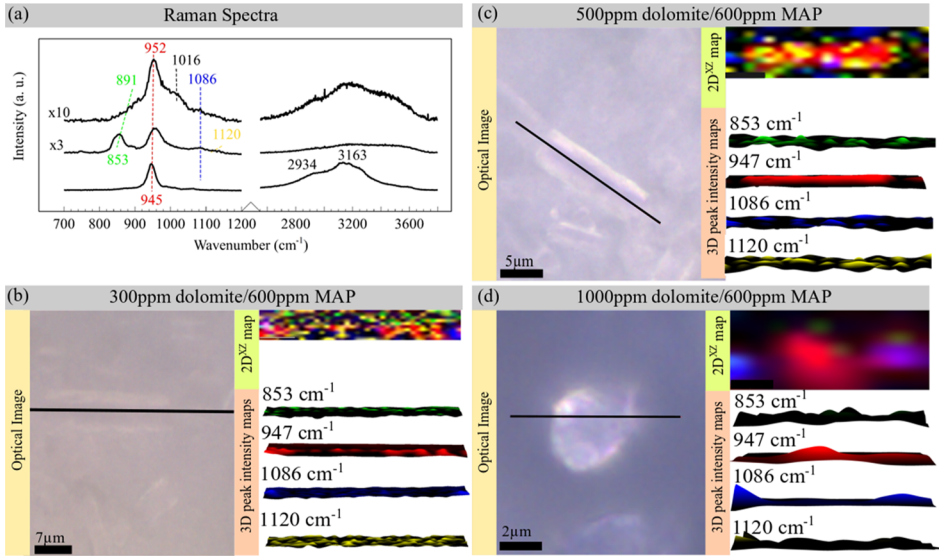

Figure 5. (a) Unique spectra measured during 2D depth Raman scans of a solid product. Unique band intensity maps were generated for the scanned single-crystal solids for 600 ppm MAP and (b) 300 ppm dolomite, (c) 500 ppm dolomite, and (d) 1000 ppm dolomite (the black line indicates the line over which the 2D scan (*xz*) was performed).

vicinity of the dolomite surface. Hence struvite crystal growth is solid dolomite particle surface-initiated.

The PO_4^{3-} adsorption data from IC measurements obeyed pseudo-second-order kinetics.[43] The plot of t/q_t versus time, as shown in Figure 4g, was used to extract the rate constants (k_2) for the pseudo-second-order process and the equilibrium PO_4^{3-} concentration (q_e) for different dolomite concentrations, as summarized in Figure 4g inset. As dolomite concentration increased from 300 to 1000 ppm, a clear decrease in equilibrium PO_4^{3-} concentration was observed. Thus, it is possible to conclude that higher dolomite concentrations lead to higher PO_4^{3-} removal, which is consistent with the IC data shown in the inset of Figure 4c. Increasing the dolomite concentration also led to an increase in the k_2 values from 3.74×10^{-5} g mg^{-1} min^{-1} at 300 ppm, to 2.63×10^{-4} g mg^{-1} min^{-1} at 500 ppm (a 7-fold increase from the 300 ppm case, even though the concentration increase was 1.7 times) to 2.21×10^{-1} at 1000 ppm (a 6000-fold increase from the 300 ppm case, even though the concentration increase was 3.3 times), which suggests that at 1000 ppm PO_4^{3-} adsorption kinetics are faster most likely due to a different PO_4^{3-} adsorption process leading toward formation of a PO_4^{3-} product other than struvite, as inferred from the larger k_2 at 1000 ppm. A previous study using MgO towards struvite growth reported q_e values of 833, 500, and 244 mg g^{-1} at 300, 500, and 1000 ppm MgO, whereas the current work with dolomite resulted in values of 1250, 909, and 476 mg g^{-1}, respectively, for 300, 500, and 1000 ppm dolomite concentrations. Therefore, at equilibrium, dolomite results in less PO_4^{3-} removal than MgO. In both the cases (MgO and dolomite), PO_4^{3-} adsorption data fit the pseudo-second-order kinetic model, which implies that like MgO, dolomite must exhibit an intermediate formation step.[10] Furthermore, the k_2 values for MgO are higher than the k_2 values for dolomite found in this study for the 300 and 500 ppm dolomite concentrations, while the k_2 value for 1000 ppm dolomite is higher than the reported k_2 of 1000 ppm MgO.[10] The k_2 value reported in the literature for MgO loaded diatomite (0.0008 mg g^{-1} min^{-1})[17] is nearly 20 times higher than the 300 ppm k_2 value for dolomite. This could be due to diatomite being a porous, high surface area material compared to the calcined dolomite.

Single Struvite Particle Compositional Analysis at the Equilibrium. The compositional variation in the product with increasing dolomite loading was investigated by using 300, 500, and 1000 ppm dolomite concentrations, which correspond to molar $[Mg^{2+}]/[NH_4^+]/[PO_4^{3-}]$ ratios of 0.41:1:1, 0.69:1:1, and 1.37:1:1, respectively, consistent with the kinetic experiments. Previous work has shown that Mg^{2+} concentration in solution affects the rate of formation of the final product.[10,19] Representative spectra obtained during depth Raman scans are shown in Figure 5a. For 300 ppm dolomite, the crystalline product exhibited a single intense Raman band at 945 cm^{-1} and a broad band with shoulders at 2934, 3163 cm^{-1}, all of which correspond to struvite Raman spectrum[10,19,66] However, some areas of the solid product also exhibited the less defined Raman spectrum with a broad, overlapping band centered at 952 cm^{-1} with shoulders at 891 and 1016 cm^{-1}, as shown in the top spectrum of Figure 5a. The 500 ppm dolomite product exhibited a single intense Raman band at 945 cm^{-1} and a broad band with shoulders at 2934, 3163 cm^{-1}, all of which correspond to struvite Raman spectrum,[10,19,66] as shown in the bottom spectrum of Figure 5a. Last, in the 1000 ppm dolomite, the solid product mostly exhibited bands at 853, ~950, 1086, and 1120 cm^{-1}, as shown in the middle spectrum of Figure 5a. A combination of possible PO_4^{3-}, HPO_4^{2-}, and $H_2PO_4^-$ species exhibit Raman bands at 853, 950, 985, and 1016 cm^{-1}, whereas CO_3^{2-} species exhibit Raman bands at 1086 cm^{-1} for $CaCO_3$ and 1120 cm^{-1} for $MgCO_3$.[10,19,65,66]

Individual band intensity analysis was conducted to elucidate heterogeneity in the single particles as shown in the 3D and 2D^{xz} plane Raman maps in Figure 5b–d. For 300 and 500 ppm dolomite, the crystalline product was of cuboid morphology (~6 μm for 300 ppm and ~15 μm for 500 ppm). However, in the case of 1000 ppm dolomite, the product was poorly crystalline with circular platelets (~3 μm) visible, as shown in the optical images in Figure 5b,c,d. Dolomite (300 ppm) exhibited localization of PO_4^{3-} (red: ~947 cm^{-1}) species, with

DOI: 10.1021/acs.jpcc.9b05292
J. Phys. Chem. C 2019, 123, 25135−25145

a significant presence of $H_2PO_4^-$ species (green: 853 cm^{-1}). Weak intensity from the $CaCO_3$ (blue: 1086 cm^{-1}) and $MgCO_3$ (yellow: 1120 cm^{-1}) species was also detected within the single crystal. The crystalline product in the case of 500 ppm dolomite showed the presence of PO_4^{3-} (947 cm^{-1}) throughout the crystal, while green inclusions (853 cm^{-1}), corresponding to lower symmetry $H_2PO_4^-$, were observed to be localized on the outer edges of the crystal. $CaCO_3$ (blue: 1086 cm^{-1}) was present mostly outside of the crystal while $MgCO_3$ (yellow: 1120 cm^{-1}) was co-localized within the solid crystals with the PO_4^{3-} species (red: 947 cm^{-1}). Last, the solid product from 1000 ppm dolomite did not exhibit any intensity from 853 and 1120 cm^{-1} bands. The scanned solid particle was homogenous and exhibited band intensity corresponding to PO_4^{3-} (red: 947 cm^{-1}). $CaCO_3$ (blue: 1086 cm^{-1}) was observed outside the circular platelet comprised of PO_4^{3-} phase, most likely present in the amorphous bulk phase.

Proposed Mechanism of Struvite Formation on the Dolomite Surface. Based on the in situ Raman spectra presented in Figure 3a,b, the spectrokinetics analysis shown in Figure 3c, and the spatially resolved ex situ single-crystal Raman maps shown in Figure 5, a qualitative model describing the observed adsorption dynamics on 800 °C calcined dolomite was derived and illustrated in Figure 6. The model

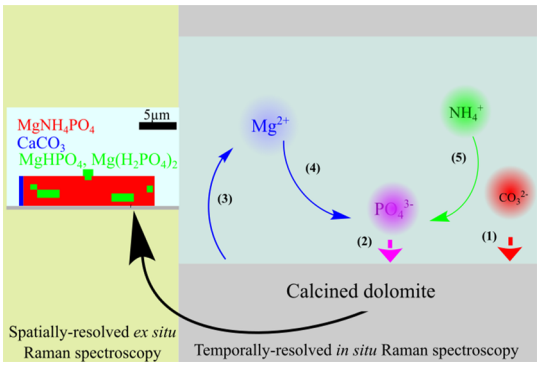

Figure 6. Proposed mechanism for struvite formation on 800 °C calcined dolomite surface in 500/600 ppm dolomite/MAP solution, based on in situ temporally resolved Raman data and spectrokinetic analysis.

can be divided into two temporal phases composed of roughly 5 steps, namely, (1) $Mg(OH)_2$- and $Ca(OH)_2$-rich dolomite hydration involving CO_3^{2-} adsorption (most likely from ambient CO_2 dissolving into the solution) onto the −OH sites, as inferred from the increase in 1086/3620 cm^{-1} band intensity ratio. Previously, similar behavior was observed when MgO was used instead of dolomite.[10] (2), PO_4^{3-} adsorption with CO_3^{2-} depletion, followed closely by the formation of $H_2PO_4^-$ and HPO_4^{2-} species on the surface. The appearance of additional Raman bands correlates directly to the loss of degeneracy within the adsorbed T_d PO_4^{3-} as the T_d symmetry of the PO_4^{3-} species is lowered[65,75] to C_{3v} (HPO_4^{2-}) and C_{2v} ($H_2PO_4^-$). Only one phosphate band at 952 cm^{-1} was present at the start of the second temporal phase, but five Raman bands were observed with time, towards the end of the second tempoeral phase, consistent with the decrease in symmetry. Data presented in Figure 4e suggest that only ∼5 ppm of Mg^{2+} ions is present in bulk aqueous phase. Hence, there is virtually no thermodynamic force to drive bulk struvite crystal precipitation in solution. Instead, supersaturation can only occur in the vicinity of the surface with any dissolved Mg^{2+} via step (3) reacting with surface-bound phosphate ions in step (4). Next, the relative intensity of Raman bands corresponding to lower symmetry $H_2PO_4^-$ and HPO_4^{2-} species decreased and the intensity of the T_d PO_4^{3-} Raman band increased, in conjunction with the appearance of NH_4^+ Raman bands in step (5), indicating struvite crystal growth.

It was intriguing to note that T_d PO_4^{3-} adsorbed species appeared first and were followed by adsorbed lower symmetry HPO_4^{2-} and $H_2PO_4^-$ species, which were succeeded by crystalline struvite ($MgNH_4PO_4$) formation. It has previously been shown using in situ micro-Raman studies of K_2HPO_4[64] and KH_2PO_4[76] droplets that in undersaturated conditions, $H_2PO_4^-$ exists as hydrated monomers ($H_2PO_4^-$−nH_2O) with pronounced ∼877 and ∼1077 cm^{-1} bands. Upon supersaturation, polymeric/dimeric $H_2PO_4^-$ chains form, indicated by asymmetric broadening, weakening, and shifting of the 1077 cm^{-1} Raman band toward lower wavenumbers.[64,76−78] Provided that in this work, the 875 and 1060 cm^{-1} Raman bands were observed in the later stages of the reaction, it can be inferred that PO_4^{3-} adsorption, and more importantly, lower symmetry $H_2PO_4^-$ (C_{2v}) ion adsorption resulted in the onset of crystalline struvite formation, under supersaturated conditions at the solid−solution boundary. The formation of such distorted, low-symmetry nucleates can be of profound importance for the crystal structure of the final struvite product. Such intermediate nucleate species most likely help in minimizing the entropic penalty for crystallization of struvite, as explained by the Ostwald step rule[79] and Spaepen's model.[76,80] According to Spaepen's model,[76,80] the nucleation barrier for a solid crystallizing is related to its configurational entropy difference between the crystal and liquid, as given by 2

$$a_T = \frac{N_i}{N}\left(\frac{\Delta S_{config}(\text{bulk}-\text{interface})}{\Delta S_{fusion}}\right) \quad (2)$$

where N_i is the number of atoms in the interface, N is the number of atoms in the crystal plane, ΔS_{config}(bulk) is the configurational entropy of the bulk crystal, ΔS_{config}(interface) is the configurational entropy of the interface, and ΔS_{fusion} is the fusion entropy per atom. This model suggests that the structural similarity between the crystal and liquid lowers crystallization barrier, which has been observed in alloys,[81−83] metals,[84,85] and, recently, in crystallization of K_2PO_4.[76,77] It can be proposed that the nucleated $H_2PO_4^-$ with symmetry lower than the T_d PO_4^{3-} might be playing a role in providing structural similarity needed to nucleate struvite crystals. Struvite crystal has a layered orthorhombic[86] structure, with PO_4^{3-} tetrahedrons, NH_4^+ tetrahedrons, and $[Mg{\cdot}6H_2O]^{2+}$ octahedrons coordinated within the unit cell with extensive hydrogen bonding, which introduces distortions.[87−89] With the supersaturation at the dolomite surface, the formation of low-symmetry local surface structures might be providing configurational similarity to the distorted units within the final struvite crystal, thereby lowering the nucleation barrier. Because the growth of struvite crystals takes place at the solid−solution interface, one expects such transformation in the local surface structures at the solid−solution boundary to play a primary role in the growth, kinetics, and morphology of the final crystalline product, as has been observed in other studies.[77]

DOI: 10.1021/acs.jpcc.9b05292
J. Phys. Chem. C 2019, 123, 25135−25145

CONCLUSIONS

This work provides a characterization of solid phases via pXRD and spatially resolved ex situ Raman spectroscopy, which showed that solid struvite exhibited chemical heterogeneities with phases such as $MgCO_3$, $CaCO_3$, $MgNH_4PO_4$, $Mg(H_2PO_4)_2$, $MgHPO_4$, present within the final crystalline product. The literature[23,90] on struvite synthesis using dolomite lacks thorough insights regarding the chemical nature of the solid product, the kinetics of struvite formation, a possible mechanism of the reaction and relies solely on the bulk crystalline analysis of the products. Recent study of spatially-resolved struvite crystal formation from $MgCO_3$ in the presence of either low-solubility $CaCO_3$ or soluble $CaCl_2$ shows kinetic hindrance of struvite formation with the latter, whereas the former resulted in phase-separated struvite/calcite particles.[19] In agreement, results of this work also show that the presence of low-solubility Ca minerals in calcined dolomite does not inhibit struvite crystal formation. Moreover, pseudo-second-order kinetics were observed for struvite formation using dolomite, with k_2 values of 3.74×10^{-5} g mg^{-1} min^{-1} at 300 ppm, 2.63×10^{-4} g mg^{-1} min^{-1} at 500 ppm, and 2.21×10^{-1} g mg^{-1} min^{-1} at 1000 ppm dolomite, although a secondary phosphate product besides struvite was formed at 1000 ppm dolomite. q_e value comparison showed that at equilibrium, dolomite resulted in less NH_4^+ and PO_4^{3-} removal than when other insoluble minerals like periclase and magnesite were used as the Mg^{2+} sources. Lastly, it was shown that dolomite had to be calcined at 800 °C, otherwise, no struvite product formed even after 2 h of reaction time. Temporally-resolved in situ Raman spectroscopy results showed that the 800 °C calcined dolomite surface had −OH functional groups that actively served as adsorption sites for CO_3^{2-}. The adsorbed CO_3^{2-} then further served as adsorption sites for PO_4^{3-}, HPO_4^{2-} and $H_2PO_4^-$ species. Adsorbed low-symmetry polymeric $H_2PO_4^-$ chains were observed on the dolomite surface at the onset of struvite crystal lattice growth, which hint that geometric adjustment of such polymeric units at the solid−solution boundary might play a crucial role in the composition, growth, and morphology of the crystalline product. These new insights into the possible mechanism of struvite formation on calcined dolomite surfaces can serve as motivation to tailor and treat precursor materials to promote struvite formation.

AUTHOR INFORMATION

Corresponding Author

*E-mail: job314@lehigh.edu. Phone: +1-610-758-6836.

ORCID

Jonas Baltrusaitis: 0000-0001-5634-955X

Author Contributions

D.K. and M.S. contributed equally. Y.S. and M.S. performed IC studies, while D.K. performed all of the Raman studies. M.S. performed pXRD studies. D.K., M.S., and J.B. performed experiment design, data analysis and wrote the manuscript.

Notes

The authors declare no competing financial interest.

ACKNOWLEDGMENTS

This material is based on work supported by the National Science Foundation under grant no. CHE 1710120.

REFERENCES

(1) Bouwman, L.; Goldewijk, K. K.; Van Der Hoek, K. W.; Beusen, A. H. W.; Van Vuuren, D. P.; Willems, J.; Rufino, M. C.; Stehfest, E. Exploring global changes in nitrogen and phosphorus cycles in agriculture induced by livestock production over the 1900-2050 period. *Proc. Natl. Acad. Sci. U.S.A.* **2013**, *110*, 20882−20887.

(2) Bouwman, L.; Goldewijk, K. K.; Van Der Hoek, K. W. Exploring global changes in nitrogen and phosphorus cycles in agriculture induced by livestock production over the 1900−2050 period. *Proc. Natl. Acad. Sci. U.S.A.* **2013**, *110*, 20882−20887.

(3) Canfield, D. E.; Glazer, A. N.; Falkowski, P. G. The Evolution and Future of Earth's Nitrogen Cycle. *Science* **2010**, *330*, 192−196.

(4) Bouwman, A. F.; Boumans, L. J. M.; Batjes, N. H. Estimation of global NH $_3$ volatilization loss from synthetic fertilizers and animal manure applied to arable lands and grasslands. *Global Biogeochem. Cycles* **2002**, *168*-18-14.

(5) Zhang, H. C.; Cao, Z. H.; Shen, Q. R.; Wong, M. H. Effect of phosphate fertilizer application on phosphorus (P) losses from paddy soils in Taihu Lake Region. *Chemosphere* **2003**, *50*, 695−701.

(6) Cordell, D.; Rosemarin, A.; Schröder, J. J.; Smit, A. L. Towards global phosphorus security: a systems framework for phosphorus recovery and reuse options. *Chemosphere* **2011**, *84*, 747−758.

(7) Lu, X.; Shih, K.; Li, X.-y.; Liu, G.; Zeng, E. Y.; Wang, F. Accuracy and application of quantitative X-ray diffraction on the precipitation of struvite product. *Water Res.* **2016**, *90*, 9−14.

(8) Foley, J. A.; Defries, R.; Asner, G. P.; Barford, C.; Bonan, G.; Carpenter, S. R.; Chapin, F. S.; Coe, M. T.; Daily, G. C.; Gibbs, H. K.; et al. Global Consequences of Land Use. *Science* **2005**, *309*, 570−574.

(9) Cai, T.; Park, S. Y.; Li, Y. Nutrient recovery from wastewater streams by microalgae: Status and prospects. *Renew. Sustain. Energy Rev.* **2013**, *19*, 360−369.

(10) Kiani, D.; Sheng, Y.; Lu, B.; Barauskas, D.; Honer, K.; Jiang, Z.; Baltrusaitis, J. Transient Struvite Formation during Stoichiometric (1:1) NH4+ and PO43- Adsorption/Reaction on Magnesium Oxide (MgO) Particles. *ACS Sustain. Chem. Eng.* **2018**, *7*, 1545−1556.

(11) Casali, L.; Mazzei, L.; Shemchuk, O.; Sharma, L.; Honer, K.; Grepioni, F.; Ciurli, S.; Braga, D.; Baltrusaitis, J. Novel Dual-Action Plant Fertilizer and Urease Inhibitor: Urea·Catechol Cocrystal. Characterization and Environmental Reactivity. *ACS Sustain. Chem. Eng.* **2019**, *7*, 2852−2859.

(12) Sharma, L.; Brigaityte, O.; Honer, K.; Kalfaoglu, E.; Slinksiene, R.; Streimikis, V.; Sviklas, A. M.; Baltrusaitis, J. Carnallite-Derived Solid Waste as Potassium (K) and Magnesium (Mg) Source in Granulated Compound NPK Fertilizers. *ACS Sustain. Chem. Eng.* **2018**, *6*, 9427−9433.

(13) Bouropoulos, N. C.; Koutsoukos, P. G. Spontaneous precipitation of struvite from aqueous solutions. *J. Cryst. Growth* **2000**, *213*, 381−388.

(14) Liu, J.; Bearden, M. D.; Fernandez, C. A.; Fifield, L. S.; Nune, S. K.; Motkuri, R. K.; Koech, P. K.; McGrail, B. P. Techno-Economic Analysis of Magnesium Extraction from Seawater via a Catalyzed Organo-Metathetical Process. *JOM* **2018**, *70*, 431−435.

(15) Al Mutaz, I. S.; Wagialia, K. M. Production of magnesiumfrom desalination brines. *Resour. Conserv. Recycl.* **1990**, *3*, 231−239.

(16) Kirinovic, E.; Leichtfuss, A. R.; Navizaga, C.; Zhang, H.; Schuttlefield Christus, J. D.; Baltrusaitis, J. Spectroscopic and Microscopic Identification of the Reaction Products and Intermediates during the Struvite (MgNH4PO4·6H2O) Formation from Magnesium Oxide (MgO) and Magnesium Carbonate (MgCO3) Microparticles. *ACS Sustain. Chem. Eng.* **2017**, *5*, 1567−1577.

(17) Xia, P.; Wang, X.; Wang, X.; Song, J.; Wang, H.; Zhang, J.; Zhao, J. Struvite crystallization combined adsorption of phosphate and ammonium from aqueous solutions by mesoporous MgO-loaded diatomite. *Colloids Surfaces A Physicochem. Eng. Asp.* **2016**, *506*, 220−227.

(18) Stolzenburg, P.; Capdevielle, A.; Teychené, S.; Biscans, B. Struvite precipitation with MgO as a precursor: Application to wastewater treatment. *Chem. Eng. Sci.* **2015**, *133*, 9−15.

DOI: 10.1021/acs.jpcc.9b05292
J. Phys. Chem. C 2019, 123, 25135−25145

(19) Lu, B.; Kiani, D.; Taifan, W.; Barauskas, D.; Honer, K.; Zhang, L.; Baltrusaitis, J. Spatially Resolved Product Speciation during Struvite Synthesis from Magnesite (MgCO3) Particles in Ammonium (NH4+) and Phosphate (PO43-) Aqueous Solutions. *J. Phys. Chem. C* **2019**, *123*, 8908.
(20) Gunay, A.; Karadag, D.; Tosun, I.; Ozturk, M. Use of magnesit as a magnesium source for ammonium removal from leachate. *J. Hazard. Mater.* **2008**, *156*, 619−623.
(21) Yu, R.; Ren, H.; Wu, J.; Zhang, X. A novel treatment processes of struvite with pretreated magnesite as a source of low-cost magnesium. *Environ. Sci. Pollut. Res.* **2017**, *24*, 22204−22213.
(22) Krähenbühl, M.; Etter, B.; Udert, K. M. Pretreated magnesite as a source of low-cost magnesium for producing struvite from urine in Nepal. *Sci. Total Environ.* **2016**, *542*, 1155−1161.
(23) Chen, L.; Zhou, C. H.; Zhang, H.; Tong, D. S.; Yu, W. H.; Yang, H. M.; Chu, M. Q. Capture and recycling of ammonium by dolomite-aided struvite precipitation and thermolysis. *Chemosphere* **2017**, *187*, 302−310.
(24) McKenzie, J. A.; Vasconcelos, C. Dolomite Mountains and the origin of the dolomite rock of which they mainly consist: historical developments and new perspectives. *Sedimentology* **2009**, *56*, 205−219.
(25) Warren, J. Dolomite: occurrence, evolution and economically important associations. *Earth Sci. Rev.* **2000**, *52*, 1−81.
(26) Broadhurst, F. M.; Howie, R. A. X-ray data for dolomite and ankerite. *Am. Mineral.* **1958**, *43*, 1210−1216.
(27) Otsuka, R. Recent studies on the decomposition of the dolomite group by thermal analysis. *Thermochim. Acta* **1986**, *100*, 69−80.
(28) Kristóf-Makó, É.; Juhász, A. Z. The effect of mechanical treatment on the crystal structure and thermal decomposition of dolomite. *Thermochim. Acta* **1999**, *342*, 105−114.
(29) Valverde, J. M.; Perejon, A.; Medina, S.; Perez-Maqueda, L. A. Thermal decomposition of dolomite under CO_2: insights from TGA and in situ XRD analysis. *Phys. Chem. Chem. Phys.* **2015**, *17*, 30162−30176.
(30) Zarghami, S.; Ghadirian, E.; Arastoopour, H.; Abbasian, J. Effect of Steam on Partial Decomposition of Dolomite. *Ind. Eng. Chem. Res.* **2015**, *54*, 20.
(31) Bénézeth, P.; Berninger, U.-N.; Bovet, N.; Schott, J.; Oelkers, E. H. Experimental determination of the solubility product of dolomite at 50-253 °C. *Geochim. Cosmochim. Acta* **2018**, *224*, 262−275.
(32) Fernández, A. I.; Chimenos, J. M.; Segarra, M.; Fernández, M. A.; Espiell, F. Kinetic study of carbonation of MgO slurries. *Hydrometallurgy* **1999**, *53*, 155−167.
(33) Sheila, D.; Sankaran, C.; Khangaonkar, P. R. Studies on the extraction of magnesia from low grade magnesites by carbon dioxide pressure leaching of hydrated magnesia. *Miner. Eng.* **1991**, *4*, 79−88.
(34) Smithson, G. L.; Bakhshi, N. N. The kinetics and mechanism of the hydration of magnesium oxide in a batch reactor. *Can. J. Chem. Eng.* **1969**, *47*, 508−513.
(35) Xing, Z.; Bai, L.; Ma, Y.; Wang, D.; Li, M. Mechanism of magnesium oxide hydration based on the multi-rate model. *Materials* **2018**, *11*, 1835.
(36) Wiechers, H. N. S. Calcium Carbonate and Magnesium Hydroxide Solubility Product Values for Heterogeneous Systems. *Eighth Int. Conf. Water Pollut. Res.* **1978**, 531−545.
(37) Johnston, J. The solubility-product constant of calcium and magnesium carbonates. *J. Am. Chem. Soc.* **1915**, *37*, 2001−2020.
(38) Le Corre, K. S.; Valsami-Jones, E.; Hobbs, P.; Parsons, S. A. Impact of calcium on struvite crystal size, shape and purity. *J. Cryst. Growth* **2005**, *283*, 514−522.
(39) Ishii, S. K. L.; Boyer, T. H. Life cycle comparison of centralized wastewater treatment and urine source separation with struvite precipitation: Focus on urine nutrient management. *Water Res.* **2015**, *79*, 88−103.
(40) Yetilmezsoy, K.; Sapci-Zengin, Z. Recovery of ammonium nitrogen from the effluent of UASB treating poultry manure wastewater by MAP precipitation as a slow release fertilizer. *J. Hazard. Mater.* **2009**, *166*, 260−269.
(41) Rahman, M. M.; Salleh, M. A. M.; Rashid, U.; Ahsan, A.; Hossain, M. M.; Ra, C. S. Production of slow release crystal fertilizer from wastewaters through struvite crystallization - A review. *Arab. J. Chem.* **2014**, *7*, 139−155.
(42) Zhang, T.; Ding, L.; Ren, H. Pretreatment of ammonium removal from landfill leachate by chemical precipitation. *J. Hazard. Mater.* **2009**, *166*, 911−915.
(43) Ho, Y. S.; McKay, G. Pseudo-second order model for sorption processes. *Process Biochem.* **1999**, *34*, 451−465.
(44) The Product Solid Phases. In *Geological Sequestration of Carbon Dioxide*; Marini, L. B. T.-D., Ed.; Elsevier, 2007; Chapter 5, Vol. *11*, pp 79−167.
(45) Rodriguez-Navarro, C.; Kudlacz, K.; Ruiz-Agudo, E. The mechanism of thermal decomposition of dolomite: New insights from 2D-XRD and TEM analyses. *Am. Mineral.* **2012**, *97*, 38−51.
(46) Sasaki, K.; Qiu, X.; Hosomomi, Y.; Moriyama, S.; Hirajima, T. Effect of natural dolomite calcination temperature on sorption of borate onto calcined products. *Microporous Mesoporous Mater.* **2013**, *171*, 1−8.
(47) Wilson, K.; Hardacre, C.; Lee, A. F.; Montero, J. M.; Shellard, L. The application of calcined natural dolomitic rock as a solid base catalyst in triglyceride transesterification for biodiesel synthesis. *Green Chem.* **2008**, *10*, 654−659.
(48) Sun, J.; Wu, Z.; Cheng, H.; Zhang, Z.; Frost, R. L. A Raman spectroscopic comparison of calcite and dolomite. *Spectrochim. Acta Part A Mol. Biomol. Spectrosc.* **2014**, *117*, 158−162.
(49) Paulo, C.; Dittrich, M. 2D Raman spectroscopy study of dolomite and cyanobacterial extracellular polymeric substances from Khor Al-Adaid sabkha (Qatar). *J. Raman Spectrosc.* **2013**, *44*, 1563−1569.
(50) Padanyi, Z. V. The Raman spectrum of Ca(OH)2. *Solid State Commun.* **1970**, *8*, 541−543.
(51) Schmid, T.; Dariz, P. Shedding light onto the spectra of lime: Raman and luminescence bands of CaO, Ca(OH)2and CaCO3. *J. Raman Spectrosc.* **2014**, *46*, 141−146.
(52) Carteret, C.; De La Pierre, M.; Dossot, M.; Pascale, F.; Erba, A.; Dovesi, R. The vibrational spectrum of CaCO3aragonite: A combined experimental and quantum-mechanical investigation. *J. Chem. Phys.* **2013**, *138*, 014201.
(53) Roelcke, M.; Han, Y.; Li, S. X.; Richter, J. Laboratory measurements and simulations of ammonia volatilization from urea applied to calcareous Chinese loess soils. *Plant Soil* **1996**, *181*, 123−129.
(54) Duffy, T. S.; Meade, C.; Fei, Y.; Mao, H.; Hemley, R. J. High-pressure phase transition in brucite, Mg(OH)2. *Am. Mineral.* **1995**, *80*, 222−230.
(55) Dawson, P.; Hadfield, C. D.; Wilkinson, G. R. The polarized infra-red and Raman spectra of Mg(OH)2 and Ca(OH)2. *J. Phys. Chem. Solids* **1973**, *34*, 1217−1225.
(56) Koutsopoulos, S. Synthesis and characterization of hydroxyapatite crystals: A review study on the analytical methods. *J. Biomed. Mater. Res.* **2002**, *62*, 600−612.
(57) Sharma, S. K.; Misra, A. K.; Clegg, S. M.; Barefield, J. E.; Wiens, R. C.; Acosta, T. E.; Bates, D. E. Remote-Raman spectroscopic study of minerals under supercritical CO2 relevant to Venus exploration. *Spectrochimica Acta—Part A: Molecular and Biomolecular Spectroscopy* **2011**, *80*, 75−81.
(58) Hazen, R. M. Effects of temperature and pressure on the cell dimension and X-ray temperature factors of periclase. *Am. Mineral.* **1976**, *61*, 266.
(59) Markgraf, S. A.; Reeder, R. J. High-temperature structure refinements of calcite and magnesite. *Am. Mineral.* **1985**, *70*, 590−600.
(60) Catti, M.; Ferraris, G.; Hull, S.; Pavese, A. Static compression and H disorder in brucite, Mg(OH)2, to 11 GPa: a powder neutron diffraction study. *Phys. Chem. Miner.* **1995**, *22*, 200−206.

DOI: 10.1021/acs.jpcc.9b05292
J. Phys. Chem. C 2019, 123, 25135−25145

(61) Desgranges, L.; Grebille, D.; Calvarin, G.; Chevrier, G.; Floquet, N.; Niepce, J.-C. Hydrogen thermal motion in calcium hydroxide: $Ca(OH)_2$. *Acta Crystallogr. Sect. B Struct. Sci.* **1993**, *49*, 812−817.
(62) Fiquet, G.; Richet, P.; Montagnac, G. High-temperature thermal expansion of lime, periclase, corundum and spinel. *Phys. Chem. Miner.* **1999**, *27*, 103−111.
(63) Carey, D. M.; Korenowski, G. M. Measurement of the Raman spectrum of liquid water. *J. Chem. Phys.* **1998**, *108*, 2669−2675.
(64) Syed, K. A.; Pang, S.-F.; Zhang, Y.; Zeng, G.; Zhang, Y.-H. Micro-Raman Observation on the HPO42- Association Structures in an Individual Dipotassium Hydrogen Phosphate (K2HPO4) Droplet. *J. Phys. Chem. A* **2012**, *116*, 1558−1564.
(65) Frost, R. L.; Musumeci, A. W.; Kloprogge, J. T.; Adebajo, M. O.; Martens, W. N. Raman spectroscopy of hydrotalcites with phosphate in the interlayer: Implications for the removal of phosphate from water. *J. Raman Spectrosc.* **2006**, *37*, 733−741.
(66) Sharma, L.; Kiani, D.; Honer, K.; Baltrusaitis, J. Mechanochemical Synthesis of Ca- and Mg-Double Salt Crystalline Materials Using Insoluble Alkaline Earth Metal Bearing Minerals. *ACS Sustain. Chem. Eng.* **2019**, *7*, 6802−6812.
(67) Xu, N.; Chen, M.; Zhou, K.; Wang, Y.; Yin, H.; Chen, Z. Retention of phosphorus on calcite and dolomite: speciation and modeling. *RSC Adv.* **2014**, *4*, 35205−35214.
(68) De Aza, P. N.; Santos, C.; Pazo, A.; De Aza, S.; Cuscó, R.; Artús, L. Vibrational Properties of Calcium Phosphate Compounds. 1. Raman Spectrum of β-Tricalcium Phosphate. *Chem. Mater.* **1997**, *9*, 912−915.
(69) Bravo-Suárez, J. J.; Srinivasan, P. D. Design characteristics of in situ and operando ultraviolet-visible and vibrational spectroscopic reaction cells for heterogeneous catalysis. *Catal. Rev.-Sci. Eng.* **2017**, *59*, 295−445.
(70) Moncada, J.; Adams, W. R.; Thakur, R.; Julin, M.; Carrero, C. A. Developing a Raman Spectrokinetic Approach To Gain Insights into the Structure-Reactivity Relationship of Supported Metal Oxide Catalysts. *ACS Catal.* **2018**, *8*, 8976−8986.
(71) Møgelberg, T. E.; Sehested, J.; Bilde, M.; Wallington, T. J.; Nielsen, O. J. Atmospheric Chemistry of CF3CFHCF3(HFC-227ea): Spectrokinetic Investigation of the CF3CFO2CF3Radical, Its Reactions with NO and NO2, and Fate of the CF3CFOCF3Radical. *J. Phys. Chem.* **1996**, *100*, 8882−8889.
(72) Aguirre, A.; Collins, S. E. Design of an optimized DRIFT cell/microreactor for spectrokinetic investigations of surface reaction mechanisms. *Mol. Catal.* **2018**, 100628.
(73) Baltrusaitis, J.; Grassian, V. H. Carbonic Acid Formation from Reaction of Carbon Dioxide and Water Coordinated to Al(OH)3: A Quantum Chemical Study. *J. Phys. Chem. A* **2010**, *114*, 2350−2356.
(74) Baltrusaitis, J.; Jensen, J. H.; Grassian, V. H. FTIR Spectroscopy Combined with Isotope Labeling and Quantum Chemical Calculations to Investigate Adsorbed Bicarbonate Formation Following Reaction of Carbon Dioxide with Surface Hydroxyl Groups on Fe2O3and Al2O3. *J. Phys. Chem. B* **2006**, *110*, 12005−12016.
(75) Bannerman, A.; Williams, R. L.; Cox, S. C.; Grover, L. M. Visualising phase change in a brushite-based calcium phosphate ceramic. *Sci. Rep.* **2016**, *6*, 1−10.
(76) Lee, S.; Wi, H. S.; Jo, W.; Cho, Y. C.; Lee, H. H.; Jeong, S.-Y.; Kim, Y.-I.; Lee, G. W. Multiple pathways of crystal nucleation in an extremely supersaturated aqueous potassium dihydrogen phosphate (KDP) solution droplet. *Proc. Natl. Acad. Sci.* **2016**, *113*, 13618−13623.
(77) Lu, G. W.; Xia, H. R.; Sun, D. L.; Zheng, W. Q.; Sun, X.; Gao, Z. S.; Wang, J. Y. Cluster formation in solid-liquid interface boundary layers of KDP studied by raman spectroscopy. *Phys. Status Solidi Appl. Res.* **2001**, *188*, 1071−1076.
(78) Lu, G. W.; Sun, X. Raman Study of Lattice Vibration Modes and Growth Mechanism of KDP Single Crystals. *Cryst. Res. Technol.* **2002**, *37*, 93−99.
(79) Ostwald, W. Studienüber die Bildung und Umwandlung fester Körper. *Z. Phys. Chem.* **1897**, *22*, 289−330.
(80) Spaepen, F. A structural model for the solid-liquid interface in monatomic systems. *Acta Metall.* **1975**, *23*, 729−743.
(81) Hornfeck, W.; Kobold, R.; Kolbe, M.; Conrad, M.; Herlach, D. Quasicrystal nucleation and Z module twin growth in an intermetallic glass-forming system. *Nat. Commun.* **2018**, *9*, 4054.
(82) Tang, C.; Harrowell, P. Anomalously slow crystal growth of the glass-forming alloy CuZr. *Nat. Mater.* **2013**, *12*, 507−511.
(83) Kang, D.-H.; Zhang, H.; Yoo, H.; Lee, H. H.; Lee, S.; Lee, G. W.; Lou, H.; Wang, X.; Cao, Q.; Zhang, D.; et al. Interfacial free energy controlling glass-forming ability of Cu-Zr alloys. *Sci. Rep.* **2014**, *4*, 1−5.
(84) Kang, D.-H.; Jeon, S.; Yoo, H.; Ishikawa, T.; Okada, J. T.; Paradis, P.-F.; Lee, G. W. Nanosized Nucleus-Supercooled Liquid Interfacial Free Energy and Thermophysical Properties of Early and Late Transition Liquid Metals. *Cryst. Growth Des.* **2014**, *14*, 1103−1109.
(85) Kelton, K. F.; Lee, G. W.; Gangopadhyay, A. K.; Hyers, R. W.; Rathz, T. J.; Rogers, J. R.; Robinson, M. B.; Robinson, D. S. First X-Ray Scattering Studies on Electrostatically Levitated Metallic Liquids: Demonstrated Influence of Local Icosahedral Order on the Nucleation Barrier. *Phys. Rev. Lett.* **2003**, *90*, 195504.
(86) Whitaker, A.; Jeffery, J. W. The crystal structure of struvite, MgNH4PO4.6H2O. *Acta Crystallogr. Sect. B* **1970**, *26*, 1429−1440.
(87) Abbona, F.; Calleri, M.; Ivaldi, G. Synthetic struvite, MgNH4PO4.6H2O: correct polarity and surface features of some complementary forms. *Acta Crystallogr. Sect. B Struct. Sci.* **1984**, *40*, 223−227.
(88) Ferraris, G.; Fuess, H.; Joswig, W. Neutron diffraction study of MgNH4PO4.6H2O (struvite) and survey of water molecules donating short hydrogen bonds. *Acta Crystallogr. Sect. B* **1986**, *42*, 253−258.
(89) Tansman, G. F.; Kindstedt, P. S.; Hughes, J. M. Minerals in food: Crystal structures of ikaite and struvite from bacterial smears on washed-rind cheese. *Can. Mineral.* **2017**, *55*, 89−100.
(90) Pesonen, J.; Myllymäki, P.; Tuomikoski, S.; Vervecken, G.; Hu, T.; Prokkola, H.; Tynjälä, P.; Lassi, U.; Pesonen, J.; Myllymäki, P.; et al. Use of Calcined Dolomite as Chemical Precipitant in the Simultaneous Removal of Ammonium and Phosphate from Synthetic Wastewater and from Agricultural Sludge. *ChemEng.* **2019**, *3*, 40.

DOI: 10.1021/acs.jpcc.9b05292
J. Phys. Chem. C 2019, 123, 25135−25145